



Zircon Eu/Eu* in Archean TTGs with implications for the role of endogenic oxidation in Archean crustal differentiation

Ming Tang ^{a,*}, Hao Chen ^a, Shuguang Song ^a, Guozheng Sun ^b, Chao Wang ^c

^a Key Laboratory of Orogenic Belt and Crustal Evolution, MOE, School of Earth and Space Sciences, Peking University, Beijing 100871, China

^b Frontiers Science Center for Deep Ocean Multispheres and Earth System, Key Lab of Submarine Geosciences and Prospecting Techniques, MOE and College of Marine Geosciences, Ocean University of China, Qingdao 266100, China

^c Department of Earth Sciences, University of Hong Kong, Pokfulam Road, Hong Kong, China



ARTICLE INFO

Associate editor: Tsuyoshi Iizuka

Keywords:

Archean TTG
Redox
Zircon Eu/Eu*
Garnet

ABSTRACT

Redox condition is key to understanding crust formation and differentiation processes. We measured Eu anomalies in zircon in the Neoarchean tonalite-trondhjemite-granodiorite rocks (TTG) from the North China Craton to infer the Eu systematics in TTG melts, which allows us to constrain the minimum melt oxidation states. We find that those TTG samples formed at medium to high pressures have less Eu depletions (high Eu/Eu*) that are comparable to those of Phanerozoic porphyry copper deposits. To generate the zircon Eu signatures in the medium to high pressure TTGs, the melt oxygen fugacity needed to be at least 0–1 log units above the Ni-NiO buffer based on our crystallization modeling. The more oxidized compositions of medium to high pressure TTGs than those of low pressure TTGs are best explained as a consequence of endogenic oxidation due to garnet retention in their sources. Our findings further support that the redox condition of felsic crustal magmas is connected to differentiation pressure or crustal thickness, and this connection holds over much of the Earth's crustal differentiation history. In the late Archean, continuous formation of such oxidized crust may have profoundly influenced volatile output from Earth's interior and oxidative weathering processes at the surface.

1. Introduction

Redox condition exerts an important control on the physical and chemical properties of magmas and the subsequent interactions of the derivative crust with the surface environment (Frost, 1991; Kress and Carmichael, 1991; McCammon, 2005; Sun and Lee, 2022). Earth's earliest felsic crust, as preserved in the rock record, primarily consists of tonalite-trondhjemite-granodiorite rocks, also known as TTG (Moyen and Martin, 2012; Palin et al., 2020). The TTG magmas are thought to be derived from remelting of basaltic lower crust or subducted slabs (Condie, 2014; Moyen and Martin, 2012). Most TTGs have undergone extensive deformation, high-grade metamorphism, or anatexis after their formation, making it difficult to extract the primary igneous signatures related to TTG magma formation (Moyen and Martin, 2012).

The redox conditions of TTGs have garnered increasing attention recently. One early study carried out by Ishihara et al. (2006) examined the magnetite abundance provided preliminary evidence of oxidized TTGs, but the complex post-magmatic alterations may complicate the interpretations based on mineralogical compositions.

Over the last couple decades, several Ce-in-zircon oxybarometers have been developed to constrain the redox conditions of felsic magmas (e.g., Burnham and Berry, 2012; Smythe and Brenan, 2016; Trail et al., 2012). Zircon as a highly refractory mineral has been regarded as one of the most reliable "messengers" from deep time. With high closure temperatures for various elements, zircon has the potential to preserve the initial magmatic signatures. However, the concentrations of light rare earth elements are extremely low in pristine zircon, so many of these Ce-in-zircon oxybarometers are highly prone to inclusion contaminations and analytical artifacts, making them practically challenging to use on complex natural samples (Zou et al., 2019). One more recent Ce-based oxybarometer was empirically calibrated by Loucks et al. (2020). This new Ce-based oxybarometer calculates magma f_{O_2} based on Ce, Ti, and U concentrations in zircon and thus circumvents the light rare earth element issues in zircon. By combining the Ce-in-zircon oxybarometers proposed by Loucks et al. (2020) and Smythe and Brenan (2016), Ge et al. (2023) provided more definitive evidence of oxidized Archean TTGs.

Besides Ce, Eu is also a multivalent rare earth element and exists as

* Corresponding author.

E-mail address: mingtang@pku.edu.cn (M. Tang).

Eu^{2+} and Eu^{3+} in magmatic systems (Weill and Drake, 1973). Owing to their higher concentrations in zircon, middle rare earth elements, including Eu, are less susceptible to inclusion contaminations and can be measured fairly well by laser-ablation inductively coupled plasma mass spectrometers (LA-ICP-MS). Eu^{2+} is compatible in plagioclase, whereas Eu^{3+} , like other trivalent rare earth elements, is incompatible in plagioclase (Ren, 2004). Thereby, plagioclase crystallization depletes Eu in the melt and thus zircon (Fig. 1A). The extent of Eu depletion also depends on the ratio of $\text{Eu}^{2+}/\text{Eu}^{3+}$ in the melt, which is a function of redox conditions. The role of redox is also at play when Eu partitions into zircon because Eu^{2+} is significantly less compatible than Eu^{3+} in the zircon lattice (Burnham and Berry, 2012), so zircon Eu/Eu^* (chondrite normalized $\text{Eu}/\sqrt{\text{Sm} \times \text{Gd}}$) increases with oxidation (Fig. 1B). Collectively, zircon Eu/Eu^* reflects the competing effects of plagioclase crystallization and melt oxidation (Trail et al., 2012). In order to use Eu systematics to understand magma redox conditions, one must evaluate the influences of plagioclase crystallization.

In this study, we explore the possibility of using Eu/Eu^* in zircon to infer the Eu systematics in Archean TTG melts, which in turn constrains the minimum oxidation states of the TTG melts. Based on these findings, we will evaluate the role of endogenic oxidation in magmatic differentiation on early Earth, driven by pressure-dependent petrologic processes. These findings also provide implications for using zircon Eu/Eu^* as a proxy for crustal thickness.

2. Brief geologic background and samples

The North China Craton is one of the largest cratons in eastern Eurasia; it consists of several Archean to Paleoproterozoic crystalline basement terranes overlain by Mesoproterozoic to late Mesozoic strata. The eastern part of the North China Craton underwent extensive lithospheric destruction in the Mesozoic (Wu et al., 2019). While the Precambrian metamorphic basement of the North China Craton is widely thought to have formed by the accretion and amalgamation of multiple continental microblocks, no consensus has been reached on the number of microblocks, and the timing and processes of amalgamation. Three representative scenarios have been proposed for the tectonic divisions of the North China Craton basement. First, Zhao et al. (2005) proposed that the metamorphic basement of the North China Craton was formed by the amalgamation of the Eastern Block and Western Block along the Trans-North China Orogen (TNCO) at ~1.85 Ga, which is widely accepted

based on geochronology, high-pressure granulites, metamorphic P-T-t paths, and deformational characteristics. Second, Kusky and Li (2003) advocated a threefold division model, in which the vast majority of the North China Craton basement was assembled via the collision of the Eastern Block and Western Block along the intervening Central orogenic belt near the end of Archean. Third, Zhai and Santosh (2011) proposed that the unified North China Craton basement was amalgamated by seven microblocks of Jiaoliao, Qianhuai, Jining, Xuchang, Ordos, Xuhuai, and Alashan along 2.7 Ga and 2.5 Ga greenstone belts.

Archean TTG magmatism was widespread in the North China Craton, and was nearly continuous from 3.0 to 2.5 Ga (Wan et al., 2023). Both detrital zircon (Dong et al., 2023) and TTG (Sun et al., 2021) age distributions peak at ~2.5 Ga in the North China Craton, suggesting that felsic magmatism was most active at ~2.5 Ga in the North China Craton, in contrast to the ~2.7 Ga maximum seen in the global distribution (e.g., Voice et al., 2011). TTG rocks older than ~3.0 Ga are sporadically distributed. Outcrops with zircon U-Pb of ~3.8 Ga have been discovered in the Anshan area (Liu et al., 1992; Song et al., 1996; Wan et al., 2023).

Our samples were collected from three localities in the Eastern Block of the North China Craton, including western Shandong, northeastern Hebei, and southwestern Liaoning (Fig. 2). The Eastern Block was suggested to have formed via amalgamation of arc-like terranes at 2.7–2.6 Ga (Kusky et al., 2016). In western Shandong, Neoarchean intrusive rocks are widely distributed with ages peaking at ~2.7 Ga and ~2.5 Ga (Jahn et al., 1988). The ~2.7 Ga TTGs are exposed in the Taian-Pingyi-Feixian areas and the ~2.5 Ga TTGs in the Taishan, Qixingtai, Yishan and Tengzhou areas. In addition to TTG gneisses, quartz diorites, monzogranites, syenogranites, and gabbros of late Neoarchean ages are also seen in this region. The early Neoarchean TTGs in western Shandong have undergone amphibolite-facies metamorphism and show stronger deformation than the late Neoarchean TTGs. Southwestern Liaoning primarily consists of Suizhong granitic terrane, which is mostly composed of TTGs with minor monzogranite and potassic granite (Wang et al., 2016). Low- to medium-grade greenstones have been reported in the northern part of the terrane. The Xingcheng TTGs were formed in the late Neoarchean and intruded by later potassic granites. Mafic magmatic enclaves are seen in the Xingcheng TTGs (Wang et al., 2016). The Archean outcrops in northeastern Hebei belong to the Jidong high-grade gneiss terrane. The Santunying gneisses consist of TTGs, granite, and charnockite. These rocks were formed at 2.55–2.50 Ga and subsequently metamorphosed in the early Paleoproterozoic (Bai et al., 2014; Nutman

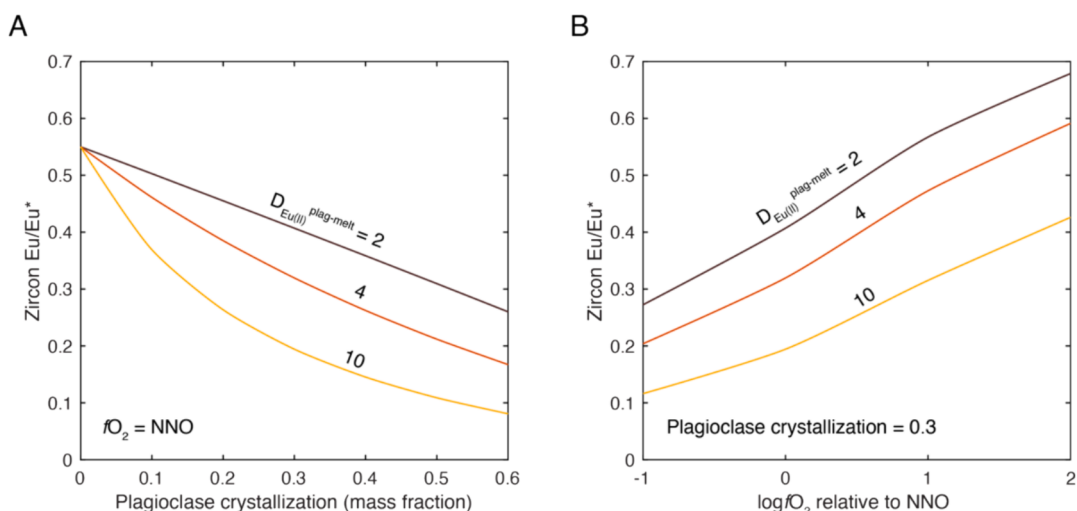


Fig. 1. The effects of plagioclase crystallization and melt oxidation on zircon Eu/Eu^* . (A) Calculated zircon Eu/Eu^* as a function of mass fraction of crystallized plagioclase. Eu^{2+} behaves similarly to Sr^{2+} , whose partition coefficient between plagioclase and melt ranges between 2 and 10 in felsic systems (data from online partition coefficient database GERM (<https://kdd.earthref.org/KdD/>)). (B) The effect of plagioclase crystallization on zircon Eu/Eu^* is strongly countered by oxidation, which converts Eu^{2+} to Eu^{3+} in the melt. The melt oxidation state is quantified as oxygen fugacity, fO_2 , relative to the Ni-NiO buffer. The relationship between melt $\text{Eu}^{2+}/\text{Eu}^{3+}$ and fO_2 is from Burnham et al. (2015).

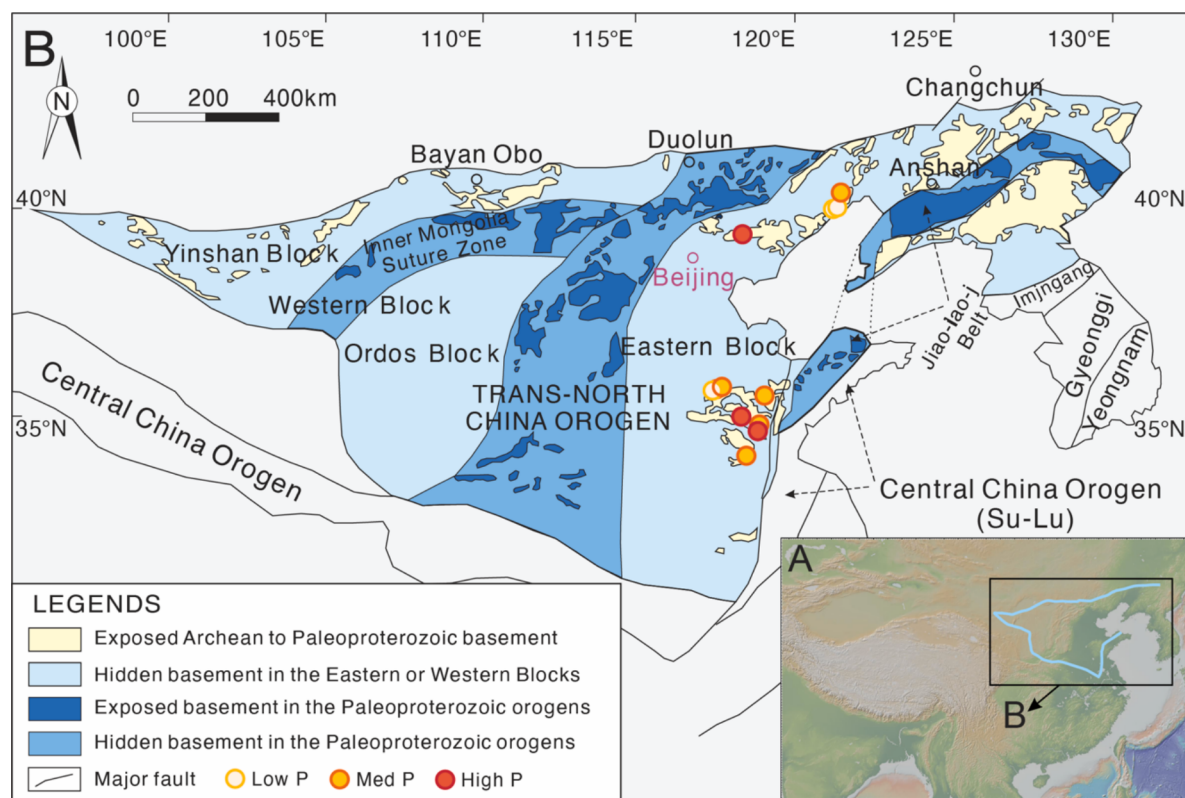


Fig. 2. Geological sketch map of the North China Craton. This map is modified from Zhao et al. (2005). The sample sites are marked by filled circles.

et al., 2011).

All of our samples plot in the TTG regime in the normative An–Ab–Or triangle diagram (Fig. S2 in Supplementary Material 1), including five granodiorites, five trondhjemites, and three tonalites. Three samples have relatively high K_2O/Na_2O ratios (~0.7). Samples 12XC-22, 12XC-28, and 10XC02 have been documented in Wang et al. (2016); samples 16SD98-1, 16SD195-1, 17SD75-4, and 16SD157-3 have been documented in Sun et al. (2019). Samples MT21-3-6, MT21-4-2, MT21-4-4, MT21-4-7, MT21-4-10, and MT21-4-11 are newly collected.

3. Analysis and data filtering

We measured zircon U–Pb isotopes and trace elements ($n = 896$) simultaneously for these samples using LA-ICP-MS. Detailed method descriptions and reference zircon measurement data are provided in Supplementary Materials 1 and 2. Zircon trace element data can be compromised by many factors, particularly for ancient samples like Archean TTGs. These samples may have undergone complex thermal events after their formation. We screened the data using a series of filters so that the remaining data best reflect the primary magmatic signatures. These filters are listed and explained in Table 1. So far, titanite is the only accessory phase known to affect the Eu/Eu* of zircon (Loader et al.,

2017).

In addition to titanite, apatite and allanite are also typical phases rich in rare earth elements. Allanite is rarely observed in our TTGs, but apatite is commonly seen. However, the partition coefficients for middle rare earth elements between apatite and silicic melts are 1–2 orders of magnitude lower than those of titanite. With a mode of <0.5 % in TTGs, apatite is thus unlikely to have a major impact on zircon Eu/Eu*.

4. Results

Our samples have SiO_2 contents of 63–72 wt% and K_2O/Na_2O ratios of 0.15–0.74 (average 0.43). Zircon U–Pb dating shows that these samples range between 2469 and 2687 Ma in age (Table 2, Fig. S5). Trace element compositions are provided in Supplementary Material 2. We used two approaches to determine the formation pressures of these samples. First, we adopted the classic approach proposed by Moyen (2011) and divided these samples into low-pressure (LP), medium-pressure (MP), and high-pressure (HP) TTGs based on their whole-rock compositions (see Section 5.3 for potential issues of this classification scheme). Second, we followed Johnson et al. (2017) and carried out combined phase equilibria and trace element modeling (Supplementary Material 1). This approach yielded consistent results with those

Table 1
Zircon trace element data filters.

Filter	Removal criteria	Notes
U–Pb discordance	>10 %	Analyses with high age discordance may have undergone significant thermal resetting. Discordance was calculated as the absolute value of $(^{206}Pb/^{238}U \text{ age} - ^{207}Pb/^{206}Pb \text{ age})/^{207}Pb/^{206}Pb \text{ age}$ (Spencer et al., 2016).
La concentration	>1 ppm	Analyses with high La concentrations may be significantly compromised by inclusions (Tang et al., 2021b).
Th/U ratio	<0.1	Analyses with extremely low Th/U may represent metamorphic zircon affected by monazite and allanite (Hoskin and Schaltegger, 2003).
Ta concentration	<0.2 ppm	Analyses with extremely low Ta concentrations may indicate significant titanite co-crystallization, which may lead to elevated Eu/Eu* in zircon (Loader et al., 2017).

Table 2

Sample ages and major element compositions.

Sample	Type	Age, Ma (± 2 se)	SiO ₂	TiO ₂	Al ₂ O ₃	FeO _T	MnO	MgO	CaO	K ₂ O	Na ₂ O	P ₂ O ₅	LOI
12XC-22*	LP	2544 ± 8	64.45	0.42	16.25	4.15	0.09	1.13	3.82	3.14	4.22	0.16	1.15
12XC-28*	LP	2533 ± 17	67.69	0.61	15.52	3.58	0.07	0.97	3.11	2.53	3.69	0.19	0.97
MT21-4-2	LP	2469 ± 23	63.45	0.65	14.46	5.10	0.07	3.72	4.58	2.53	3.77	0.18	1.06
16SD98-1†	MP	2544 ± 15	69.21	0.39	15.29	3.52	0.06	1.42	2.68	2.23	3.94	0.17	0.60
16SD195-1†	MP	2536 ± 6	72.13	0.20	15.26	1.91	0.03	0.68	2.98	0.78	5.28	0.03	0.41
17SD75-4†	MP	2569 ± 87	68.44	0.35	15.22	3.59	0.05	1.69	2.59	1.45	5.17	0.13	0.79
10XC02*	MP	2500 ± 20	70.84	0.47	14.44	2.78	0.03	1.49	0.76	1.30	6.49	0.23	1.32
MT21-4-4	MP	2647 ± 9	63.96	0.50	15.83	4.28	0.06	2.86	4.77	1.62	4.31	0.14	1.23
MT21-4-7	MP	2687 ± 14	67.68	0.40	16.02	3.39	0.04	1.07	3.34	1.36	4.83	0.15	1.38
16SD157-3†	HP	2660 ± 8	72.03	0.33	14.67	2.63	0.03	0.95	2.86	2.03	3.78	0.08	0.21
MT21-4-10	HP	2599 ± 27	71.40	0.22	15.81	1.43	0.03	0.56	2.23	2.26	5.47	0.08	0.50
MT21-4-11	HP	2598 ± 25	72.19	0.18	15.43	1.16	0.02	0.42	1.98	2.64	5.11	0.06	0.57
MT21-3-6†	HP	2547 ± 8	68.80	0.38	15.16	3.48	0.04	1.69	3.76	1.07	4.68	0.11	0.80

Notes:

* Whole-rock data from Wang et al. (2016).

† Whole-rock data from Sun et al. (2019).

from Moyen's approach and showed that our studied LP-, MP-, and HP-TTGs formed at 5–6 kbar, 8–12 kbar, and >14 kbar, respectively (Fig. S6). These pressure conditions are broadly consistent with previous experimental (Moyen and Stevens, 2006) and modeling studies (Johnson et al., 2017; Sun et al., 2021). In addition, we plotted zircon Eu/Eu* vs. whole-rock La/Yb and Sr/Y ratios for our TTG samples (Fig. 4). Both La/Yb and Sr/Y ratios have been widely used to indicate the differentiation pressure of granitic rocks (Chapman et al., 2015; Chiaradia, 2015; Profeta et al., 2015).

MP- and HP-TTGs have systematically higher zircon Eu/Eu* than LP-TTGs (Fig. 3A). In LP-TTGs, most zircon Eu/Eu* are lower than 0.3; in MP- and HP-TTGs, median zircon Eu/Eu* generally fall between 0.4 and 0.6. The difference in zircon Eu/Eu* is less discernible between MP- and HP-TTGs. Our data also show overall positive, though noisy, correlations between zircon Eu/Eu* and whole-rock La/Yb and Sr/Y ratios (Fig. 4).

5. Discussion

The zircon Eu/Eu* in MP- and HP-TTGs are significantly higher than those of Phanerozoic regular granites unassociated with ore deposits but comparable to those seen in porphyry Cu deposits (Fig. 3B and C). More importantly, porphyry Cu intrusions are generally oxidized with $\log f_{\text{O}_2} \geq \text{NNO} + 0.5$ (Richards, 2015). We thus ask a question whether the high zircon Eu/Eu* seen in the Archean MP- and HP-TTGs also requires oxidized melt composition.

5.1. Minimum f_{O_2} of TTG melts constrained by zircon Eu/Eu*

The high zircon Eu/Eu* in MP- and HP-TTGs could result from either suppression of plagioclase crystallization or oxidized melt compositions. Below, we couple rhyolite-MELTS simulations (Gualda et al., 2012) and a zircon saturation model (Boehnke et al., 2013) to constrain the effects

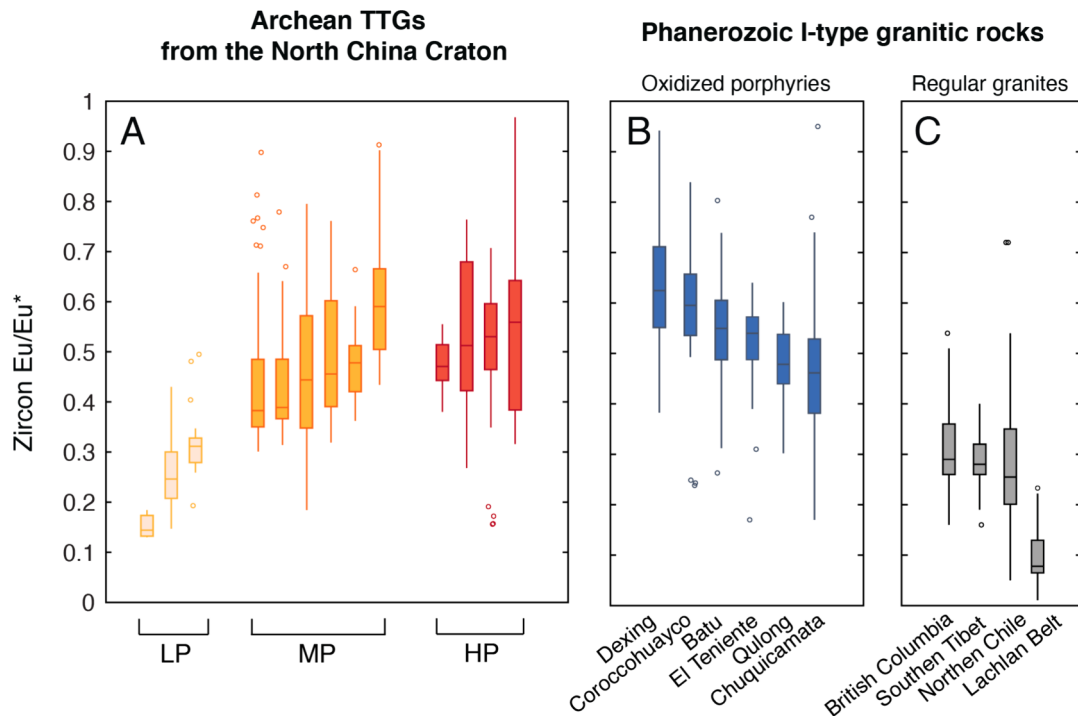


Fig. 3. Zircon Eu/Eu* in North China Craton TTGs and representative Phanerozoic I-type granitic rocks. The data are shown as box and whisker plots. The ends of the boxes show the upper and lower quartiles, and the ends of the whiskers show the 2.5 and 97.5 percentiles. Outliers are plotted as individual points. The data sources of Phanerozoic porphyry Cu deposits and regular granites (not associated with porphyry Cu deposits) are provided in Supplementary Material 2.

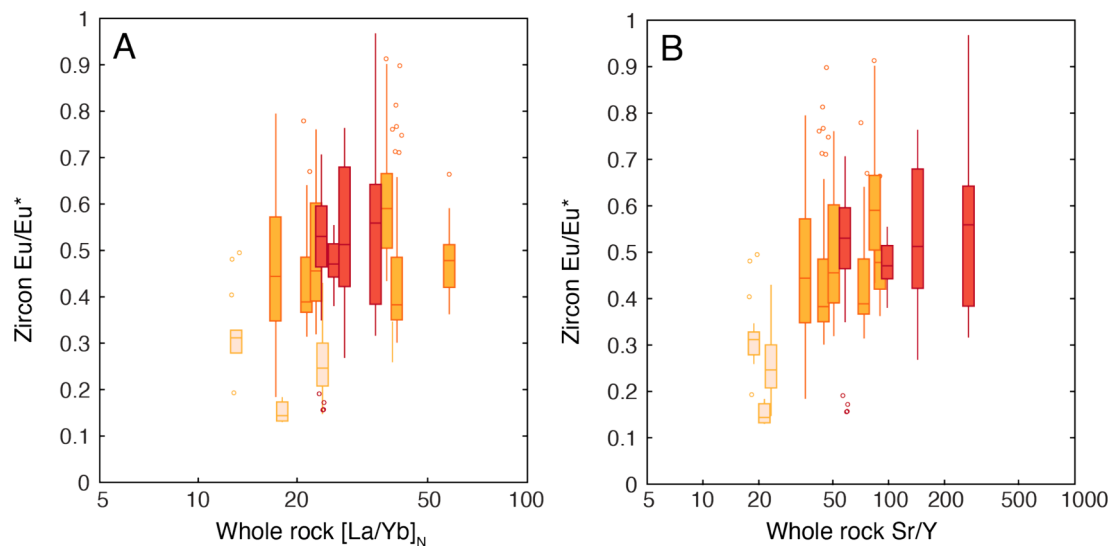


Fig. 4. Zircon Eu/Eu* vs. whole-rock La/Yb (chondrite normalized) and Sr/Y ratios for the studied TTG samples. Similar to Fig. 3, the data are shown as box and whisker plots.

of plagioclase crystallization and redox conditions on zircon Eu/Eu*. Both rhyolite-MELTS simulations and trace element modeling were done in the batch mode. The purpose of this modeling exercise is to access whether plagioclase fractionation/crystallization alone can account for the range of zircon Eu/Eu* observed in the studied Archean TTGs.

We assume that most zircon grains crystallized in shallow magma chambers that formed TTG plutons. These shallow magma chambers were fed by parental TTG melts derived from basalt remelting in the deep crust (Moyen and Martin, 2012). The composition of the parental TTG melt is hard to constrain. Our simulations consider three end-member parental melt compositions—average TTG (Moyen and Martin, 2012), primitive TTG melt (Laurent et al., 2020), and evolved TTG melt (Laurent et al., 2020).

The plagioclase effect on zircon Eu/Eu* occurs through two mechanisms: plagioclase fractionation/retention in the deep crustal sources and plagioclase co-crystallization in the shallow magma chamber. To account for the influence of plagioclase fractionation/retention in the source, we vary Eu/Eu* in the parental melt from 0.5 to 1. For this part, we do not model the processes that cause plagioclase fractionation/retention or the amount of residual plagioclase in the source; all we need for the subsequent crystallization model is the resultant Eu/Eu* in the parental TTG melt (x-axes in Figs. 5 and 6). Plagioclase crystallization in the shallow magma chamber will continue to change Eu/Eu* in the melt. This constantly changing melt Eu/Eu* will be picked up by the crystallizing zircon crystals, and therefore, zircon will record a range of Eu/Eu*. To account for plagioclase co-crystallization in the shallow magma chamber, we calculate Eu/Eu* evolution in continuously crystallizing zircon as a function of plagioclase crystallization simulated by rhyolite-MELTS (Supplementary Material 1). Then, we compare these calculated Eu/Eu* distributions in zircon that crystallizes throughout the pluton solidification with those observed in TTGs. Below, we describe the calculations in more details.

The crystallization results from the rhyolite-MELTS simulations (Supplementary Material 2) were used to quantify melt Eu/Eu* using the classic batch crystallization model (Eq. (1)).

$$C_l/C_o = [F(1 - D) + D]^{-1} \quad (1)$$

where, C_l and C_o are the concentrations of the element of interest in the remaining and original liquids, respectively; F is melt fraction; D is partition coefficient.

The plagioclase crystallization effect on melt Eu/Eu* depends on Eu²⁺/Eu³⁺ in the melt and the partition coefficient of Eu²⁺ between

plagioclase and melt ($D_{\text{Eu}^{2+}}^{\text{plag}}$). Eu²⁺/Eu³⁺ in the melt can be described by the relationship from Burnham et al. (2015):

$$\frac{\text{Eu}^{3+}}{\sum \text{Eu}} = \frac{1}{1 + 10^{-0.25\log O_2 - \frac{6410}{T} - 14.2\Lambda} + 10.1} \quad (2)$$

where T is temperature in K, Λ is optical basicity, which can be estimated from melt major element compositions (Duffy, 1993) and is ~0.54 for the average TTG composition. $D_{\text{Eu}^{2+}}^{\text{plag}}$ can be approximated by $D_{\text{Sr}}^{\text{plag}}$. A survey of the online partition coefficient database GERM shows $D_{\text{Sr}}^{\text{plag}}$ in the range of 2–10. In our calculations, we adopt $D_{\text{Sr}}^{\text{plag}} = 2$. With this lower bound value, our calculated melt Eu depletion due to plagioclase crystallization represents a minimum estimate, which in turn will lead to a minimum estimate of melt fO_2 . Trivalent REEs are incompatible in plagioclase (Aigner-Torres et al., 2007; Ren, 2004). A survey of the partition coefficient database GERM database shows that $D_{\text{Sm}}^{\text{plag}}$ and $D_{\text{Gd}}^{\text{plag}}$ generally range between 0.05 and 0.2 for felsic systems. In our model, we arbitrarily set $D_{\text{Eu}^{3+}}^{\text{plag}} = 0.1$. We also assume that non-plagioclase phases have bulk $D_{\text{Eu}^{2+}}^{\text{non-plag}} = D_{\text{Eu}^{3+}}^{\text{non-plag}} = 0.5$. This assumption is based on the consideration that middle REEs are generally moderately incompatible and that Sm, Eu, and Gd are not substantially fractionated by non-plagioclase phases (e.g., Davidson et al., 2007). Our sensitivity tests show that the uncertainties in these trivalent REE partition coefficients have negligible influences on the modeled zircon Eu/Eu* (Fig. S7).

Zircon crystallization in the magma chamber can be modeled using an experimentally calibrated zircon saturation model (Boehnke et al., 2013):

$$\ln D_{\text{Zr}}^{\text{zircon}} = 10108/T - 1.16*(M - 1) - 1.48 \quad (3)$$

where D_{Zr} is the distribution coefficient of Zr between zircon and melt. M is a melt composition parameter whose value can be calculated from rhyolite-MELTS simulation outputs after each step of crystallization. Zircon Eu/Eu* can be calculated as:

$$\begin{aligned} (\text{Eu}/\text{Eu}^*)_{\text{zircon}} &= (\text{Eu}/\text{Eu}^*)_{\text{melt}} * (\text{Eu}^{3+}/\Sigma \text{Eu})_{\text{melt}} \\ &\quad * D_{\text{Eu}^{2+}}^{\text{zircon}} / \sqrt{D_{\text{Sm}}^{\text{zircon}} \times D_{\text{Gd}}^{\text{zircon}}} + (\text{Eu}^{2+}/\Sigma \text{Eu})_{\text{melt}} \\ &\quad * D_{\text{Eu}^{2+}}^{\text{zircon}} / \sqrt{D_{\text{Sm}}^{\text{zircon}} \times D_{\text{Gd}}^{\text{zircon}}} \end{aligned} \quad (4)$$

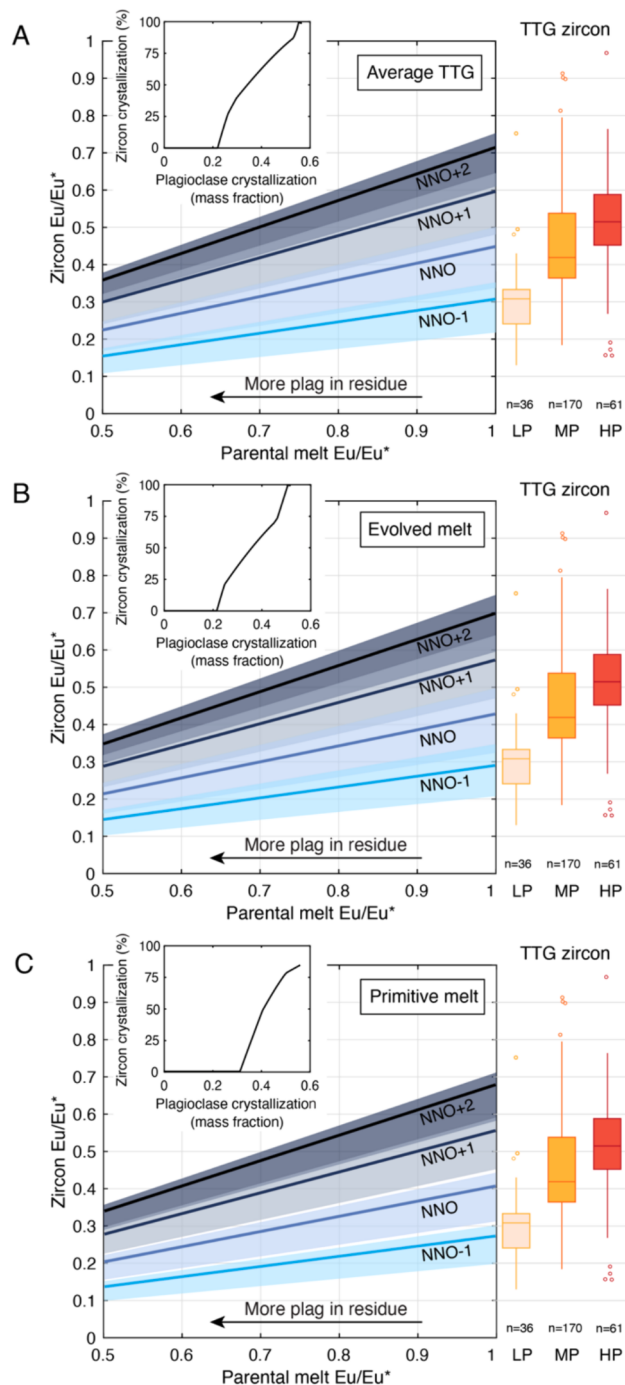


Fig. 5. Modeled zircon Eu/Eu* distributions compared with measured zircon Eu/Eu* distributions of TTGs. This modeling exercise allows us to evaluate what combinations of parental melt Eu/Eu* and redox conditions may explain the zircon Eu/Eu* distributions observed in LP-, MP- and HP-TTGs. The calculated zircon Eu/Eu* distributions are shown by the lines (medians) and bracketing bands (1st and 3rd quartiles). The spread in zircon Eu/Eu* is due to plagioclase co-crystallization during pluton solidification. Parental melt Eu/Eu* reflects residual plagioclase in deep crustal sources. (A), (B), and (C) represent modeling results using three endmember parental melt compositions for crystallization simulations (see texts). The inset in each panel shows the simulated zircon and plagioclase co-crystallization in the shallow magma chamber. On the right-hand side of each panel, we plot the distributions of zircon Eu/Eu* measured in LP-, MP- and HP-TTGs as boxes and whiskers similar to those in Fig. 3. This set of crystallization simulations were run under 2 kbar pressure and 4 wt% initial melt water content. However, we find that pressure and water have limited effects on the simulation results (Fig. 6).

Because Eu will not be fractionated from Sm and Gd when Eu is 100 % Eu³⁺, $D_{\text{Eu}^{3+}}^{\text{zircon}} / \sqrt{D_{\text{Sm}}^{\text{zircon}} \times D_{\text{Gd}}^{\text{zircon}}} = 1$. We further assumed that $D_{\text{Eu}^{2+}}^{\text{zircon}} / \sqrt{D_{\text{Sm}}^{\text{zircon}} \times D_{\text{Gd}}^{\text{zircon}}} = 1$ because Eu²⁺, like Sr, is highly incompatible in zircon (Burnham and Berry, 2012). Eq. (4) can be simplified to:

$$(\text{Eu}/\text{Eu}^*)_{\text{zircon}} = (\text{Eu}/\text{Eu}^*)_{\text{melt}} * (\text{Eu}^{3+}/\Sigma\text{Eu})_{\text{melt}} \quad (5)$$

Combining Eqs. (2) and (5), we can derive the relationships between zircon Eu/Eu*, melt Eu/Eu*, and $f\text{O}_2$. This relationship, coupled with plagioclase and zircon crystallization simulations described above, links zircon Eu/Eu* distribution to parental melt Eu/Eu* and $f\text{O}_2$.

Fig. 5 shows the results of simulations run at 2 kbar pluton crystallization pressure and 4 wt% initial water content. For any given parental melt Eu/Eu* and $f\text{O}_2$ conditions, our model returns a spread in zircon Eu/Eu* with progressive crystallization. The spread in zircon Eu/Eu* results from plagioclase co-crystallization as expected. The modeled zircon Eu/Eu* distributions are plotted as medians and 1st and 3rd quartiles (Fig. 5). Overall, zircon Eu/Eu* increases with increasing parental melt Eu/Eu* and $f\text{O}_2$. Although most zircon Eu/Eu* values can be obtained by adjusting parental melt Eu/Eu* and $f\text{O}_2$, the high zircon Eu/Eu* observed in many MP- and HP-TTGs require a combination of near-unity Eu/Eu*, or no Eu anomaly, in the parental melt and oxidized conditions, between NNO and NNO+1. This means that merely suppressing plagioclase effect in the deep crustal residue is insufficient to account for the high zircon Eu/Eu* in MP- and HP-TTGs, as well as those granitic magmas associated with Phanerozoic porphyry Cu deposits.

Any decrease in parental melt Eu/Eu* (due to residual plagioclase in the source) would require even higher $f\text{O}_2$. Take Fig. 5A for example, if the parental TTG melt has an Eu/Eu* of 1 (no residual plagioclase in the source), the TTG melt will need to have an $f\text{O}_2$ equivalent to ~NNO to crystallize zircon with a median Eu/Eu* matching that of MP-TTGs; if the parental TTG melt has an Eu/Eu* of 0.7 (some residual plagioclase in the source), the melt will need an $f\text{O}_2$ of ~NNO + 1 to crystallize zircon with a similar Eu/Eu* distribution. This conclusion remains valid for all three parental melt scenarios (Fig. 5). Given that the Eu/Eu* of the parental TTG melt is likely ≤ 1 , an $f\text{O}_2$ of 0–1 log units above the NNO buffer represents the minimum oxidation state inferred for the MP- and HP-TTGs.

Because plagioclase saturation can be suppressed by high pressure and high water contents, we also ran the simulations at 1–5 kbar and 2–10 wt% initial water content (Ge et al., 2023) to evaluate the sensitivity of the crystallization model. These additional simulations show that the uncertainties in crystallization pressure and magma water content have limited influences on zircon Eu/Eu* and the estimation of minimum $f\text{O}_2$ (Fig. 6). Increasing water content and pressure only slightly reduce the amount of crystallized plagioclase at 75 % zircon crystallization. This is likely because, for a highly differentiated system like TTG magmas, plagioclase is the most important crystallizing phase whose crystallization strongly controls the compositional evolution of the remaining melt, including its Zr concentration. Zircon crystallization is thus closely connected to plagioclase crystallization after pluton emplacement.

The modeling approach discussed above has several important uncertainties/caveats. We now evaluate these uncertainties/caveats and how they may affect the modeling results.

First of all, rhyolite-MELTS has issues in modeling amphibole crystallization because some minor components that serve to stabilize amphibole relative to pyroxene are not included in the models of the MELTS family (<https://magmasource.caltech.edu/forum/index.php?topic=833.0>). This is not a critical issue in our calculations because amphibole and other non-plagioclase minerals in TTGs do not fractionate Eu from Sm and Gd significantly (Davidson et al., 2007; Ren, 2004). So, the failure to model amphibole crystallization bears no influence on the calculated zircon Eu/Eu* distributions.

Second, plagioclase accumulation is another important process in the

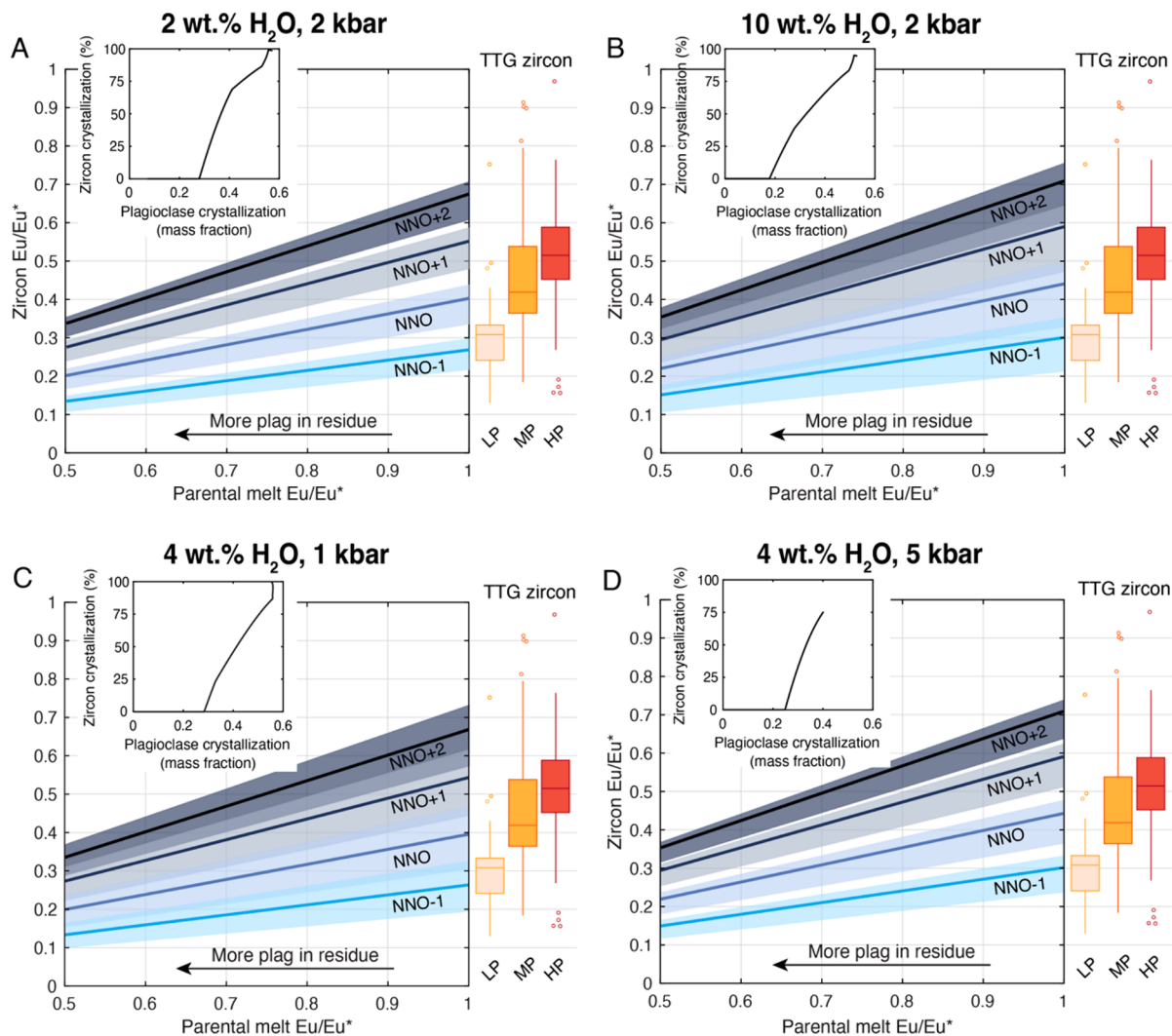


Fig. 6. Water and pressure effects on plagioclase-zircon co-crystallization and zircon Eu/Eu* distributions. This group of simulations used the average TTG composition as that of the parental melt. A and B were run at a constant pressure of 2 kbar and 2 and 10 wt% initial water contents. C and D were run at 4 wt% initial water content and 1 and 5 kbar crystallization pressures. Similar to Fig. 5, the lines and bracketing bands show the medians and 1st and 3rd quartiles of the calculated zircon Eu/Eu* distributions, respectively.

formation of TTGs (Laurent et al., 2020). Plagioclase accumulation results from solid-melt segregation, and the loss of low Eu/Eu* melt increases Eu/Eu* of the residual mush. Some TTG samples displaying whole-rock Eu/Eu* > 1 may represent solidified mush materials after various extents of melt loss. While this process may be important to determining the whole-rock compositions, it bears no direct influence on trace element partitioning between the remaining melt and solid phases, and thus will not affect Eu/Eu* in the melt and zircon as long as they remain in equilibrium. In other words, zircon trace elements can see through solid-melt segregation process.

Third, the melt Eu²⁺/Eu³⁺ – $f\text{O}_2$ relationship used here was calibrated based on a suite of experiments done at 1250–1500 °C (Burnham et al., 2015), a temperature range that is higher than that of typical TTG magmas. Without new experiments, we cannot critically evaluate how reliable this extrapolation is. But we note that the relationship between Eu²⁺/Eu³⁺, $f\text{O}_2$, melt composition, and temperature was calibrated based on a thermodynamic formula (Burnham et al., 2015). Thus, extrapolation of this melt Eu²⁺/Eu³⁺ – $f\text{O}_2$ relationship to lower temperatures is not an unguessed endeavor.

To summarize, MP- and HP-TTGs from the North China Craton appear to be oxidized with a lower bound $f\text{O}_2$ of NNO to NNO+1. The oxidized nature of many Archean TTGs was also shown by several recent

studies (Ge et al., 2023; Meng et al., 2022). Specifically, Ge et al. (2023) applied two Ce-based oxybarometers to TTG zircon and found that the $f\text{O}_2$ of TTG melts may have been as high as FMQ + 1, similar to our results. Meng et al. (2022) examined S oxidation state in apatite from the Superior Province TTGs. Their data show that sulfate may have been abundant in many TTG magmas.

5.2. Comparison with zircon Ce-(U-Ti)-oxybarometer results

Ge et al. (2023) used two zircon Ce-based oxybarometers (Loucks et al., 2020; Smythe and Brenan, 2016) to study the redox conditions of the Archean TTGs. Their redox results were obtained by the zircon Ce-(U-Ti)-oxybarometer calibrated by Loucks et al. (2020), whereas the other zircon Ce-based oxybarometer established by Smythe and Brenan (2016) was used as a hydrometer to constrain the water content in the TTG melt. It is interesting to note that the $f\text{O}_2$ calculated by Ge et al. (2023) positively correlates with differentiation proxies such as whole-rock Y content and La/Yb ratio but with substantial data scattering. Here we also calculated the $f\text{O}_2$ for our TTGs using the zircon Ce-(U-Ti)-oxybarometer (Loucks et al., 2020) (Fig. 7). Ignoring one sample with <5 effective paired analyses, the average $f\text{O}_2$ calculated from the zircon Ce-(U-Ti)-oxybarometer roughly correlates with average zircon Eu/Eu*,

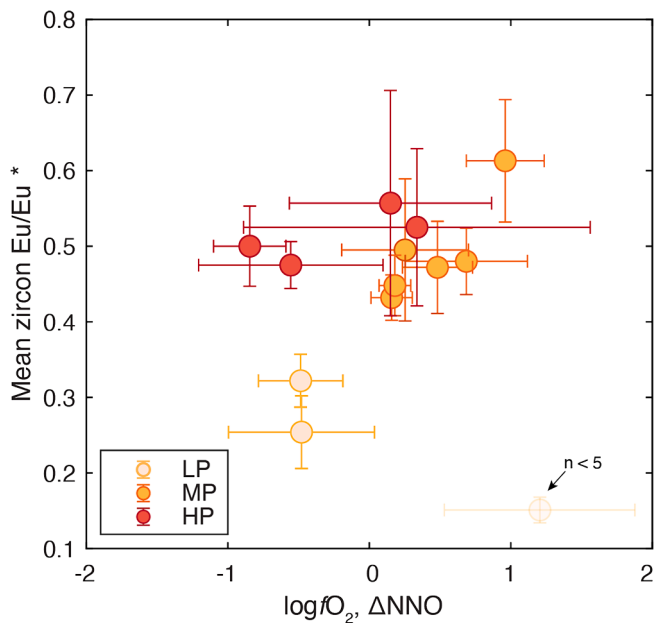


Fig. 7. Mean zircon Eu/Eu* vs. $f\text{O}_2$ calculated from zircon Ce-(U-Ti)-oxybarometer (Loucks et al., 2020). One LP sample is dimmed for its limited paired zircon analyses after data filtering ($n = 4$). Based on our petrologic modeling, LP-TTGs have a minimum $f\text{O}_2$ of NNO-1 to NNO, whereas MP- and HP-TTGs have a minimum $f\text{O}_2$ of NNO to NNO + 1 (Fig. 5).

which also depends on $f\text{O}_2$ as modeled and discussed in Section 5.1. However, this correlation is notably noisy, likely due to two reasons discussed below.

First, the average zircon Eu/Eu* may only be used to constrain the minimum $f\text{O}_2$. Second, to use Loucks et al.'s oxybarometer, the influence of magmatic differentiation on $f\text{O}_2$ calculation needs to be quantified and corrected for. Loucks et al. (2020) did so using the U/Ti ratio in zircon as a differentiation index. Loucks et al. (2020) examined magmatic rocks from a variety of tectonic settings and found that magma $\log(\text{Ce}/\text{U})$ linearly correlates with $\log(\text{U}/\text{Ti})$ with a slope of ~ -0.5 . This slope of -0.5 was then used in their formulation of the oxybarometer. However, we examined a larger igneous database for modern arc magmas and found that the slope of $\log(\text{Ce}/\text{U})$ vs. $\log(\text{U}/\text{Ti})$ correlation is not constant. In particular, in arcs where crustal thickness exceeds 50 km, the average slope of $\log(\text{Ce}/\text{U})$ vs. $\log(\text{U}/\text{Ti})$ correlation is only half of that of thinner arcs (-0.34 vs. -0.68 , Fig. S8). This crustal thickness dependence is probably a consequence of pressure control on magmatic differentiation (Chen et al., 2023). For example, the crystallization of oxides is sensitive to differentiation pressure (Tang et al., 2019; Tang et al., 2023). We do not intend to discount the Ce-based oxybarometer calibrated by Loucks et al. (2020), which is useful for discerning large redox variations. However, the use of constant slope of $\log(\text{Ce}/\text{U})$ vs. $\log(\text{U}/\text{Ti})$ correlation may blur the results when the samples of interest have a limited $f\text{O}_2$ range ($<\sim 2$ log units), and particularly when that $f\text{O}_2$ variation may be related to magmatic differentiation pressure as we will discuss below.

5.3. Oxidation mechanism of Archean TTGs

The oxidized nature of MP- and HP-TTGs seems peculiar. These TTGs, particularly MP-TTGs, are abundant in the late Archean felsic crust. In the Phanerozoic, high $f\text{O}_2$ magmas are mostly seen in subduction zones. The oxidized nature of many arc magmas is usually attributed to the incorporation of subducted oxidized surface materials (Fe^{3+} and S^{6+} bearing phases) in the sources (Kelley and Cottrell, 2009), although this mechanism is highly debated (e.g., Lee et al., 2010). This exogenic oxidation depends on the availability and recycling of oxidized

surface materials. In the Archean, Earth's surface was highly reduced with detrital pyrite and uranite commonly seen in sedimentary successions (Johnson et al., 2014; Lyons et al., 2014). Although "oxygen oases" may have existed locally in some isolated shallow ocean environments (Eickmann et al., 2018), the deep ocean remained anoxic (Lyons et al., 2014; Stolper and Keller, 2018).

One clue may come from the observation that only MP- and HP-TTGs are oxidized whereas LP-TTGs are not. It should be noted that all TTG classification schemes based on whole-rock compositions may be compromised by solid-melt segregation processes. Melt loss or plagioclase accumulation increases La/Yb, Sr/Y, and K/Na ratios of TTGs (Laurent et al., 2020), which are important criteria in the LP-, MP-, and HP-TTG classification schemes (Moyen, 2011). However, if the compositional diversity of TTGs was generated solely by solid-melt segregation, it would be difficult to explain the systematic difference in zircon Eu/Eu* between LP-TTGs and MP- and HP-TTGs (Figs. 3 and 4). We suggest that, while the compositional differences between MP- and HP-TTGs may be explained by solid-melt segregation processes, the petrogenetic processes that formed the MP- and HP-TTGs are distinct from those forming the LP-TTGs. We further suggest that the oxidized compositions of MP- and HP-TTGs resulted from pressure controlled endogenic oxidation, which also likely occurred in the formation of Phanerozoic porphyry Cu intrusions (Lee and Tang, 2020; Tang et al., 2020).

Endogenic oxidation may arise as a basaltic crust undergoes partial melting at high pressure, with abundant garnet in the melting residues. This garnet is typically rich in the almandine component, with high Fe contents but very low $\text{Fe}^{3+}/\sum\text{Fe}$ (Tang et al., 2019). Garnet retention leads to a high $\text{Fe}^{3+}/\sum\text{Fe}$ and thus oxidation of the melt (Sun and Lee, 2022; Tang et al., 2018; Tang et al., 2020). This mechanism is also appealing because it provides a simple explanation for the increasing minimum $f\text{O}_2$ from LP- to MP- and HP-TTGs, as garnet retention is only possible in the sources of MP- and HP-TTGs (Fig. S6) (Moyen, 2011).

Although the oxidation effect of garnet crystallization has been modeled in several papers (Sun and Lee, 2022; Tang et al., 2018; Tang et al., 2020), precise garnet-melt Fe partition coefficient data were lacking when these calculations were done. Here we use the recent experimentally determined partition coefficients for Fe^{2+} and Fe^{3+} in garnet (Holycross and Cottrell, 2023) to recalculate the extent of oxidation due to garnet retention during basalt melting. As a proof of concept, we follow Tang et al. (2018)'s simplification and assume that the melting residue contains various proportions of garnet and non-garnet phases. Non-garnet phases have bulk Fe^{2+} and Fe^{3+} partition coefficients of 1 and 0.8, respectively. We further assume that partial melting occurs at 900 °C and the basaltic protolith has a $\text{Fe}^{3+}/\sum\text{Fe}$ of 0.1 before melting. Fig. 8 shows the calculated $f\text{O}_2$ as a function of garnet mode in the melting residue and melt fraction (F). As garnet mode increases, $f\text{O}_2$ can increase by > 2 log units—similar to the conclusions of Tang et al. (2018).

By integrating the calculated $f\text{O}_2$ (Fig. 8) with the crystallization model (Fig. 5), we now evaluate to what extent garnet retention in the source may influence the Eu/Eu* distributions recorded by zircon crystallizing from a solidifying TTG pluton. As the proportion of residual plagioclase increases, zircon Eu/Eu* decreases systematically (Fig. 9). But increasing the proportion of residual garnet counters this plagioclase effect and increases zircon Eu/Eu* due to the oxidation effect of garnet retention. Assuming no plagioclase in the melting residue, 0.1–0.2 by mode residual garnet can result in zircon Eu/Eu* comparable to those seen in MP- and HP-TTGs.

It is also worth noting that as the residual garnet mode increases, there is an initial rapid rise in both $f\text{O}_2$ and zircon Eu/Eu*, followed by a gradual flattening of the trend (Figs. 8 and 9). This result may also explain why the difference in zircon Eu/Eu* between MP- and HP-TTGs is less pronounced compared to that between LP- and MP-TTGs (Fig. 3).

Amphibole crystallization is another petrologic process that has also been proposed to cause magma oxidation (Zhang et al., 2022). However, due to the more compatible behavior of Fe^{3+} in amphibole, amphibole

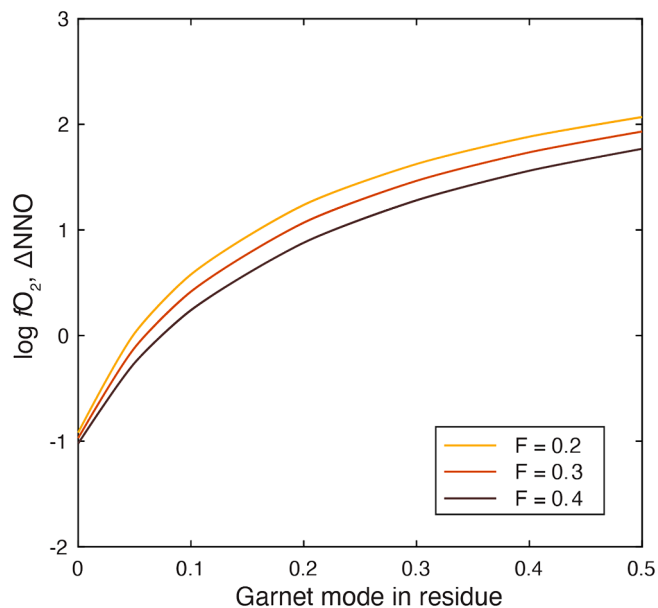


Fig. 8. Modeled oxidation effect due to garnet retention during basalt partial melting. In this model, we utilize the latest experimentally determined garnet-melt partition coefficients from Holycross and Cottrell (2023).

generally has a higher $Fe^{3+}/\sum Fe$ than that of garnet and only induces oxidation after the melt is already fairly oxidized with an $Fe^{3+}/\sum Fe > \sim 0.2$ (Zhang et al., 2022). We thus suggest that the oxidation effect associated with amphibole crystallization is limited in Archean TTG formation.

Water dissociation and diffusive loss of H may also cause oxidation of hydrous magmas (Tollan and Hermann, 2019). This mechanism was invoked by Meng et al. (2022) to explain the presence of sulfate in Archean TTG magmas. However, the increasing sulfur content in apatite, reflecting increasing sulfate content in the melt, with increasing differentiation pressure/crustal thickness revealed by their data, also hints at the role of garnet fractionation in driving TTG magma oxidation. Future studies may further explore the roles of oxidation induced by garnet crystallization and kinetic processes in Archean crustal differentiation.

5.4. Implications for the oxidation state of the Archean emerged crust

Our findings bear important implications for the nature of Earth's early continents. In the Archean, the oceanic crust may have been much thicker than today, up to 25–35 km thick due to greater mantle melting degrees (Herzberg et al., 2010). This thick oceanic crust alone would require the continental crust to be substantially thicker than today to rise above the Archean sea level based on isostasy considerations. A crust of this thickness may stabilize a significant amount (20–40 wt% of residue) of garnet in the melting residues near the Moho (Moyen and Martin, 2012; Sun et al., 2021).

The thick Archean oceanic crust may have acted as an elevation “filter” for the early continents. Continents emerging from the Archean oceans (if the continents could emerge) would reach the thickness required by endogenic oxidation. Whatever the mechanisms of orogenesis in the Archean, if the crustal thickening process was also accompanied by widespread magmatism, voluminous oxidized felsic magmas would form, which would then rise and constitute an important part of the emerged crusts. These considerations suggest that the redox evolution of Earth's continental crust may be decoupled from that of Earth's surface. Endogenic oxidation, driven by petrologic processes, may have been an important mechanism regulating the compositional architecture of the Archean continental crust.

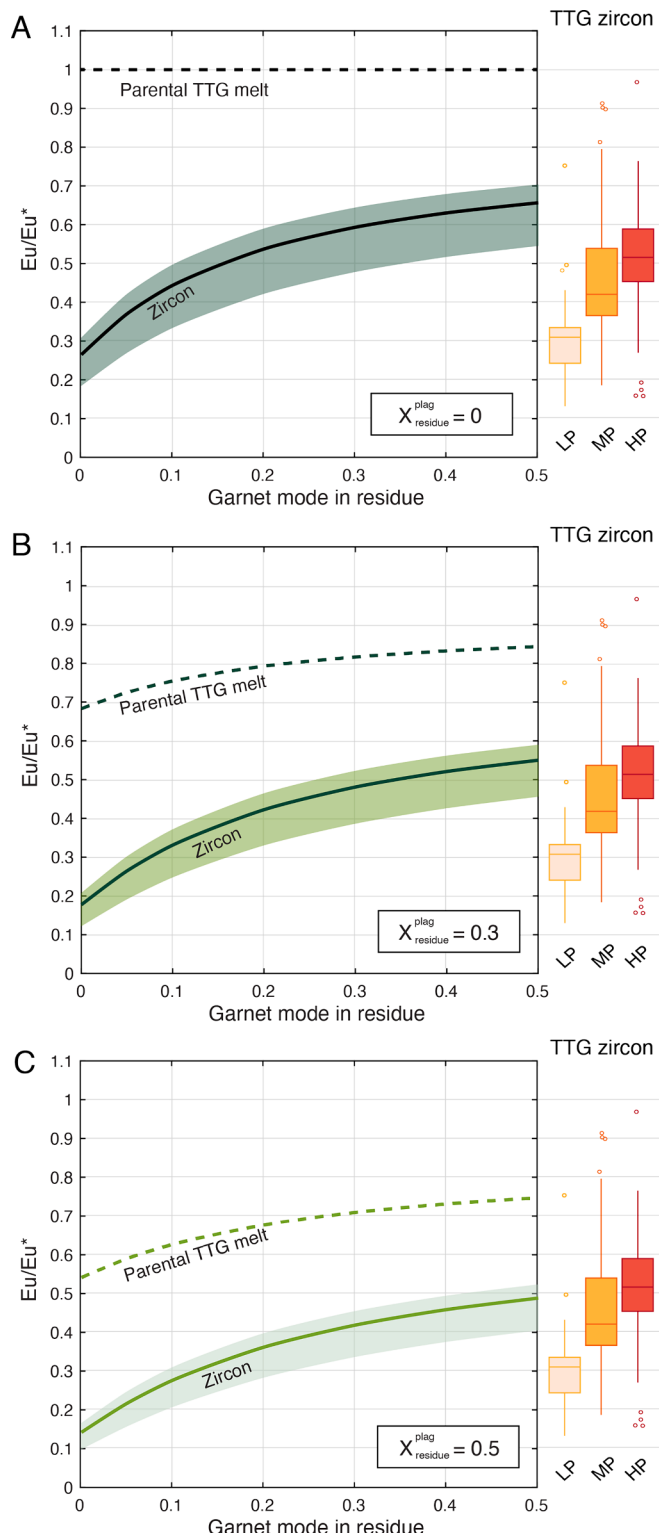


Fig. 9. Modeled zircon Eu/Eu* distributions as a function of proportions of garnet and plagioclase in the melting residue. Similar to Figs. 5 and 6, the calculated zircon Eu/Eu* distributions are plotted as medians bracketed by the 1st and 3rd quartile envelopes (lines and bands, respectively). The three panels show the calculated zircon Eu/Eu* with different modes of residual plagioclase in the source ($X_{\text{residue}}^{\text{plag}}$). In this calculation, we assumed a melt fraction of 0.3.

A growing body of evidence suggests that felsic subaerial crust expanded rapidly by the end of the Archean (Bindeman et al., 2018; Tang et al., 2016). The widespread emergence of such oxidized landmass would shield the surface environment from massive reduced Fe in Earth's lithosphere. For example, endogenic oxidation would lead to an increase in fO_2 of at least 1–2 log units, which would in turn reduce the Fe^{2+}/Fe^{3+} in TTG melts by a minimum factor of 1.6–2.5. The fundamental change in oxidative weathering capacity of the crust may have contributed to shifting the redox balance of Earth's surface near the Archean-Proterozoic boundary (Lee et al., 2016).

5.5. Implications for zircon Eu/Eu* as a crustal thickness proxy

Eu/Eu^* in zircon has been used as a proxy for crustal thickness in recent studies (e.g., Brudner et al., 2022; Tang et al., 2021a; Tang et al., 2021b). This proxy was calibrated based on the prominent correlation between zircon Eu/Eu^* and whole rock La/Yb in granitic rocks. As discussed in Tang et al. (2021b) and shown in Fig. 1, Eu/Eu^* in zircon is controlled by both plagioclase fractionation and redox. Of the two, plagioclase fractionation is widely known to be pressure-dependent (e.g., Green, 1982).

The role of redox appears to complicate the use of Eu/Eu^* in zircon to constrain magmatic differentiation pressure/crustal thickness (Trantafyllou et al., 2022; Yakymchuk et al., 2023). However, our findings here lend support to the hypothesis that the oxidation state of a felsic magma is also strongly controlled by differentiation pressure. At low pressure ($<\sim 1$ GPa), where magnetite can fractionate abundantly, the derivative melt becomes more reduced with differentiation; at high pressure ($>\sim 1$ GPa), where garnet is stable, endogenic oxidation operates and the derivative melt becomes progressively oxidized with differentiation (Sun and Lee, 2022; Tang et al., 2018; Tang et al., 2019). This pressure-dependence of oxidation is clearly seen in the Gangdese belt of southern Tibet, where S in apatite records a significant increase in magma fO_2 after extensive crustal thickening due to the Eurasia-India continental collision (Tang et al., 2020).

Collectively, although both redox condition and differentiation pressure influence zircon Eu/Eu^* , the redox condition of a felsic magma may also be a function of differentiation pressure, which in turn depends on crustal thickness. Therefore, felsic crustal melts formed from high-pressure differentiation are naturally oxidized.

6. Conclusions

We studied the whole-rock composition, zircon U-Pb age, and zircon trace element compositions for the Neoarchean TTGs from the North China Craton. Our data show that MP- and HP-TTGs have systematically higher zircon Eu/Eu^* than LP-TTGs and are similar to those of Phanerozoic porphyry Cu deposits.

Based on petrologic modeling, we find that merely suppressing plagioclase retention/fractionation in the sources cannot generate the high zircon Eu/Eu^* in MP- and HP-TTGs. Instead, these high zircon Eu/Eu^* require the parental melts of MP- and HP-TTGs to be oxidized, with minimum fO_2 of NNO to NNO + 1.

We suggest that the oxidation of MP- and HP-TTG melts was endogenic for two considerations. First, oxidized supracrustal materials were scarce in the Archean, making large scale oxidation of Earth's deep crust and mantle via supracrustal material subduction less likely. Second, the oxidation appears to correlate with formation pressure. The endogenic oxidation was likely driven by garnet retention/fractionation in the deep crust, which explains the pressure-dependence of the oxidation process. These findings highlight the role of differentiation pressure on the redox conditions of felsic magmas throughout Earth's history.

CRediT authorship contribution statement

Ming Tang: Writing – original draft, Visualization, Resources,

Project administration, Methodology, Investigation, Funding acquisition, Formal analysis, Data curation, Conceptualization. Hao Chen: Writing – review & editing, Visualization, Methodology, Formal analysis, Data curation. Shuguang Song: Writing – review & editing, Investigation. Guozheng Sun: Writing – review & editing, Visualization, Investigation. Chao Wang: Writing – review & editing, Methodology.

Declaration of competing interest

The authors declare that they have no known competing financial interests or personal relationships that could have appeared to influence the work reported in this paper.

Data availability

Data Availability Data are available through Mendeley Data at <https://doi.org/10.17632/65vpj37gv9.1>.

Acknowledgements

We thank three anonymous reviewers and Editor Tsuyoshi Iizuka for their constructive and thoughtful comments, which significantly improved our manuscript. This work was financially supported by National Natural Science Foundation of China (grants 42073026, 42125302, 41888101, and 42202220). M. Tang is grateful for the support from the New Cornerstone Science Foundation through the XPLORER PRIZE.

Appendix A. Supplementary material

Supplementary material to this article can be found online at <https://doi.org/10.1016/j.gca.2024.06.031>.

References

- Aigner-Torres, M., Blundy, J., Ulmer, P., Pettke, T., 2007. Laser Ablation ICPMS study of trace element partitioning between plagioclase and basaltic melts: an experimental approach. *Contrib. Miner. Petrol.* 153 (6), 647–667.
- Bai, X., Liu, S., Guo, R., Zhang, L., Wang, W., 2014. Zircon U-Pb-Hf isotopes and geochemistry of Neoproterozoic dioritic-trondhjemite gneisses, Eastern Hebei, North China Craton: constraints on petrogenesis and tectonic implications. *Precambr. Res.* 251, 1–20.
- Bindeman, I.N., Zakharov, D.O., Palandri, J., Greber, N.D., Dauphas, N., Retallack, G.J., Hofmann, A., Lackey, J.S., Bekker, A., 2018. Rapid emergence of subaerial landmasses and onset of a modern hydrologic cycle 2.5 billion years ago. *Nature* 557 (7706), 545–548.
- Boehnke, P., Watson, E.B., Trail, D., Harrison, T.M., Schmitt, A.K., 2013. Zircon saturation re-revised. *Chem. Geol.* 351, 324–334.
- Brudner, A., Jiang, H., Chu, X., Tang, M., 2022. Crustal thickness of the Grenville orogen: a Mesoproterozoic Tibet? *Geology* 50 (4), 402–406.
- Burnham, A.D., Berry, A.J., 2012. An experimental study of trace element partitioning between zircon and melt as a function of oxygen fugacity. *Geochim. Cosmochim. Acta* 95, 196–212.
- Burnham, A.D., Berry, A.J., Halse, H.R., Schofield, P.F., Cibin, G., Mosselmans, J.F.W., 2015. The oxidation state of europium in silicate melts as a function of oxygen fugacity, composition and temperature. *Chem. Geol.* 411, 248–259.
- Chapman, J.B., Dueca, M.N., DeCelles, P.G., Profeta, L., 2015. Tracking changes in crustal thickness during orogenic evolution with Sr/Y: an example from the North American Cordillera. *Geology* 43 (10), 919–922.
- Chen, K., Tang, M., Hu, Z., Liu, Y., 2023. Generation of tholeiitic and calc-alkaline arc magmas and its implications for continental growth. *Geochim. Cosmochim. Acta* 355, 173–183.
- Chiaradia, M., 2015. Crustal thickness control on Sr/Y signatures of recent arc magmas: an Earth scale perspective. *Scientific reports* 5.
- Condie, C.K., 2014. How to make a continent: thirty-five years of TTG research. In: Dilek, Y., Furnes, H. (Eds.), *Evolution of Archean Crust and Early Life*. Springer, Netherlands, Dordrecht, pp. 179–193.
- Davidson, J., Turner, S., Handley, H., Macpherson, C., Dosseto, A., 2007. Amphibole “sponge” in arc crust? *Geology* 35 (9), 787–790.
- Dong, Y., Zuo, P., Xiao, Z., Zhao, Y., Zheng, D., Sun, F., Li, Y., 2023. A database of detrital zircon U-Pb ages in the North China Craton from the Paleoproterozoic to the early Palaeozoic. *Geosci. Data J* n/a/n/a (n/a).
- Duffy, J.A., 1993. A review of optical basicity and its applications to oxidic systems. *Geochim. Cosmochim. Acta* 57 (16), 3961–3970.

- Eickmann, B., Hofmann, A., Wille, M., Bui, T.H., Wing, B.A., Schoenberg, R., 2018. Isotopic evidence for oxygenated Mesoarchaean shallow oceans. *Nat. Geosci.* 11 (2), 133.
- Frost, B.R., 1991. Introduction to oxygen fugacity and its petrologic importance. *Rev. Mineral. Geochem.* 25 (1), 1–9.
- Ge, R.-F., Wilde, S.A., Zhu, W.-B., Wang, X.-L., 2023. Earth's early continental crust formed from wet and oxidizing arc magmas. *Nature*.
- Green, T., 1982. Anatexis of mafic crust and high pressure crystallization of andesite. *Am. Soc. Mech. Eng. (paper)* 465–487.
- Gualda, G.A.R., Ghiorsor, M.S., Lemons, R.V., Carley, T.L., 2012. Rhyolite-MELTS: a modified calibration of MELTS optimized for silica-rich, fluid-bearing magmatic systems. *J. Petrol.* 53 (5), 875–890.
- Herzberg, C., Condie, K., Korenaga, J., 2010. Thermal history of the Earth and its petrological expression. *Earth Planet. Sci. Lett.* 292 (1–2), 79–88.
- Holycross, M., Cottrell, E., 2023. Garnet crystallization does not drive oxidation at arcs. *Science* 380 (6644), 506–509.
- Hoskin, P.W., Schaltegger, U., 2003. The composition of zircon and igneous and metamorphic petrogenesis. *Rev. Mineral. Geochem.* 53 (1), 27–62.
- Ishihara, S., Ohmoto, H., Anhaeusser, C.R., Imai, A., Robb, L.J., 2006. Discovery of the oldest oxic granitoids in the Kaapvaal Craton and its implications for the redox evolution of early Earth. *Geol. Soc. Am. Mem.* 198, 67–80.
- Jahn, B., Auvray, B., Shen, Q., Liu, D., Zhang, Z., Dong, Y., Ye, X., Zhang, Q., Cornichet, J., Mace, J., 1988. Archean crustal evolution in China: the Taishan complex, and evidence for juvenile crustal addition from long-term depleted mantle. *Precambr. Res.* 38 (4), 381–403.
- Johnson, T.E., Brown, M., Gardiner, N.J., Kirkland, C.L., Smithies, R.H., 2017. Earth's first stable continents did not form by subduction. *Nature* 543 (7644), 239–242.
- Johnson, J.E., Gerpheiide, A., Lamb, M.P., Fischer, W.W., 2014. O₂ constraints from Paleoproterozoic detrital pyrite and uraninite. *Bulletin* 126(5–6), 813–830.
- Kelley, K.A., Cottrell, E., 2009. Water and the oxidation state of subduction zone magmas. *Science* 325 (5940), 605–607.
- Kress, V.C., Carmichael, I.S., 1991. The compressibility of silicate liquids containing Fe₂O₃ and the effect of composition, temperature, oxygen fugacity and pressure on their redox states. *Contrib. Miner. Petrol.* 108 (1), 82–92.
- Kusky, T.M., Li, J., 2003. Paleoproterozoic tectonic evolution of the North China Craton. *J. Asian Earth Sci.* 22 (4), 383–397.
- Kusky, T.M., Polat, A., Windley, B.F., Burke, K.C., Dewey, J.F., Kidd, W.S.F., Maruyama, S., Wang, J.P., Deng, H., Wang, Z.S., Wang, C., Fu, D., Li, X.W., Peng, H.T., 2016. Insights into the tectonic evolution of the North China Craton through comparative tectonic analysis: a record of outward growth of Precambrian continents. *Earth Sci. Rev.* 162, 387–432.
- Laurent, O., Björnsen, J., Wotzlaw, J.-F., Bretscher, S., Silva, M.P., Moyen, J.-F., Ulmer, P., Bachmann, O., 2020. Earth's earliest granitoids are crystal-rich magma reservoirs tapped by silicic eruptions. *Nat. Geosci.* 1–7.
- Lee, C.-T.-A., Luffi, P., Le Roux, V., Dasgupta, R., Albarede, F., Leeman, W.P., 2010. The redox state of arc mantle using Zn/Fe systematics. *Nature* 468 (7324), 681–685.
- Lee, C.-T.-A., Tang, M., 2020. How to make porphyry copper deposits. *Earth Planet. Sci. Lett.* 529, 115868.
- Lee, C.-T.-A., Yeung, L.Y., McKenzie, N.R., Yokoyama, Y., Ozaki, K., Lenardic, A., 2016. Two-step rise of atmospheric oxygen linked to the growth of continents. *Nat. Geosci.* 9 (6), 417–424.
- Liu, D.Y., Nutman, A.P., Compston, W., Wu, J.S., Shen, Q.H., 1992. Remnants of ≥3800 Ma crust in the Chinese part of the Sino-Korean craton. *Geology* 20 (4), 339–342.
- Loader, M.A., Wilkinson, J.J., Armstrong, R.N., 2017. The effect of titanite crystallisation on Eu and Ce anomalies in zircon and its implications for the assessment of porphyry Cu deposit fertility. *Earth Planet. Sci. Lett.* 472, 107–119.
- Loucks, R.R., Fiorentini, M.L., Henriquez, G.J., 2020. New magmatic oxybarometer using trace elements in zircon. *J. Petrol.* 61 (3), egaa034.
- Lyons, T.W., Reinhard, C.T., Planavsky, N.J., 2014. The rise of oxygen in Earth's early ocean and atmosphere. *Nature* 506 (7488), 307–315.
- McCammon, C., 2005. The paradox of mantle redox. *Science* 308 (5723), 807–808.
- Meng, X., Simon, A.C., Kleinsasser, J.M., Mole, D.R., Kontak, D.J., Jugo, P.J., Mao, J., Richards, J.P., 2022. Formation of oxidized sulfur-rich magmas in Neoarchean subduction zones. *Nat. Geosci.* 15 (12), 1064–1070.
- Moyen, J.-F., 2011. The composite Archean grey gneisses: Petrological significance, and evidence for a non-unique tectonic setting for Archean crustal growth. *Lithos* 123 (1–4), 21–36.
- Moyen, J.-F., Martin, H., 2012. Forty years of TTG research. *Lithos* 148, 312–336.
- Moyen, J.F., Stevens, G., 2006. Experimental constraints on TTG petrogenesis: implications for Archean geodynamics. *Archean Geodyn. Environ.* 149–175.
- Nutman, A.P., Wan, Y., Du, L., Friend, C.R., Dong, C., Xie, H., Wang, W., Sun, H., Liu, D., 2011. Multistage late Neoarchean crustal evolution of the North China Craton, eastern Hebei. *Precambr. Res.* 189 (1–2), 43–65.
- Palin, R.M., Santos, M., Cao, W., Li, S.-S., Hernández-Uribe, D., Parsons, A., 2020. Secular change and the onset of plate tectonics on Earth. *Earth Sci. Rev.* 207, 103172.
- Profeta, L., Ducea, M.N., Chapman, J.B., Paterson, S.R., Gonzales, S.M.H., Kirsch, M., Petrescu, L., DeCelles, P.G., 2015. Quantifying crustal thickness over time in magmatic arcs. *Sci. Rep.* 5.
- Ren, M., 2004. Partitioning of Sr, Ba, Rb, Y, and LREE between alkali feldspar and peraluminous silicic magma. *Am. Mineral.* 89 (8–9), 1290–1303.
- Richards, J.P., 2015. The oxidation state, and sulfur and Cu contents of arc magmas: implications for metallogeny. *Lithos* 233, 27–45.
- Smythe, D.J., Brenan, J.M., 2016. Magmatic oxygen fugacity estimated using zircon-melt partitioning of cerium. *Earth Planet. Sci. Lett.* 453, 260–266.
- Song, B., Nutman, A.P., Liu, D., Wu, J., 1996. 3800 to 2500 Ma crustal evolution in the Anshan area of Liaoning Province, northeastern China. *Precambr. Res.* 78 (1–3), 79–94.
- Spencer, C.J., Kirkland, C.L., Taylor, R.J., 2016. Strategies towards statistically robust interpretations of in situ U-Pb zircon geochronology. *Geosci. Front.* 7 (4), 581–589.
- Stolper, D.A., Keller, C.B., 2018. A record of deep-ocean dissolved O₂ from the oxidation state of iron in submarine basalts. *Nature* 553 (7688), 323–327.
- Sun, C., Lee, C.-T.-A., 2022. Redox evolution of crystallizing magmas with CHOS volatiles and its implications for atmospheric oxygenation. *Geochim. Cosmochim. Acta* 338, 302–321.
- Sun, G., Liu, S., Santosh, M., Gao, L., Hu, Y., Guo, R., 2019. Thickness and geothermal gradient of Neoarchean continental crust: Inference from the southeastern North China Craton. *Gondw. Res.* 73, 16–31.
- Sun, G., Liu, S., Cawood, P.A., Tang, M., van Hunen, J., Gao, L., Hu, Y., Hu, F., 2021. Thermal state and evolving geodynamic regimes of the Meso- to Neoarchean North China Craton. *Nat. Commun.* 12 (1), 3888.
- Tang, M., Chen, K., Rudnick, R.L., 2016. Archean upper crust transition from mafic to felsic marks the onset of plate tectonics. *Science* 351 (6271), 372–375.
- Tang, M., Erdman, M., Eldridge, G., Lee, C.-T.-A., 2018. The redox "filter" beneath magmatic orogens and the formation of continental crust. *Sci. Adv.* 4 (5).
- Tang, M., Lee, C.-T.-A., Costin, G., Höfer, H.E., 2019. Recycling reduced iron at the base of magmatic orogens. *Earth Planet. Sci. Lett.* 528, 115827.
- Tang, M., Lee, C.-T.-A., Ji, W.-Q., Wang, R., Costin, G., 2020. Crustal thickening and endogenic oxidation of magmatic sulfur. *Sci. Adv.* 6 (31), eaba6342.
- Tang, M., Chu, X., Hao, J., Shen, B., 2021a. Orogenic quiescence in Earth's middle age. *Science* 371 (6530), 728–731.
- Tang, M., Ji, W.-Q., Chu, X., Wu, A., Chen, C., 2021b. Reconstructing crustal thickness evolution from europium anomalies in detrital zircons. *Geology* 49 (1), 76–80.
- Tang, M., Liu, X., Chen, K., 2023. High Mg# of the continental crust explained by calc-alkaline differentiation. *Natl. Sci. Rev.* 10 (3).
- Tollan, P., Hermann, J., 2019. Arc magmas oxidized by water dissociation and hydrogen incorporation in orthopyroxene. *Nat. Geosci.* 12 (8), 667–671.
- Trail, D., Bruce Watson, E., Tailby, N.D., 2012. Ce and Eu anomalies in zircon as proxies for the oxidation state of magmas. *Geochim. Cosmochim. Acta* 97, 70–87.
- Triantafyllou, A., Ducea, M., Jepson, G., Hernández-Montenegro, J., Bisch, A., Ganne, J., 2022. European anomalies in detrital zircons record major transitions in Earth geodynamics at 2.5 Ga and 0.9 Ga. *Geology*.
- Voice, P.J., Kowalewski, M., Eriksson, K.A., 2011. Quantifying the timing and rate of crustal evolution: global compilation of radiometrically dated detrital zircon grains. *J. Geol.* 119 (2), 109–126.
- Wan, Y., Dong, C., Xie, H., Wilde, S.A., Liu, S., Li, P., Ma, M., Li, Y., Wang, Y., Wang, K., Liu, D., 2023. Hadean to early Mesoarchean rocks and zircons in the North China Craton: a review. *Earth Sci. Rev.* 243, 104489.
- Wang, C., Song, S., Niu, Y., Wei, C., Su, L., 2016. TTG and potassic granitoids in the eastern North China Craton: making Neoarchean upper continental crust during micro-continental collision and post-collisional extension. *J. Petrol.* 57 (9), 1775–1810.
- Weill, D.F., Drake, M.J., 1973. Europium anomaly in plagioclase feldspar: experimental results and semiquantitative model. *Science* 180 (4090), 1059–1060.
- Wu, F.-Y., Yang, J.-H., Xu, Y.-G., Wilde, S.A., Walker, R.J., 2019. Destruction of the North China Craton in the Mesozoic. *Annu. Rev. Earth Planet. Sci.* 47 (1), 173–195.
- Yakymchuk, C., Holder, R.M., Kendrick, J., Moyen, J.-F., 2023. Europium anomalies in zircon: a signal of crustal depth? *Earth Planet. Sci. Lett.* 622, 118405.
- Zhai, M.-G., Santosh, M., 2011. The early Precambrian odyssey of the North China Craton: a synoptic overview. *Gondw. Res.* 20 (1), 6–25.
- Zhang, J., Wang, R., Hong, J., 2022. Amphibole fractionation and its potential redox effect on arc crust: evidence from the Kohistan arc cumulates. *Am. Mineral.* 107 (9), 1779–1788.
- Zhao, G., Sun, M., Wilde, S.A., Sanzhong, L., 2005. Late Archean to Paleoproterozoic evolution of the North China Craton: key issues revisited. *Precambr. Res.* 136 (2), 177–202.
- Zou, X., Qin, K., Han, X., Li, G., Evans, N.J., Li, Z., Yang, W., 2019. Insight into zircon REE oxy-barometers: a lattice strain model perspective. *Earth Planet. Sci. Lett.* 506, 87–96.